crystals

MDPI

Article

Evaluation of $La_{1-x}Sr_xNi_{0.4}Fe_{0.6}O_{3-\delta}$ as Electrode Materials for Direct Methane Symmetrical Solid Oxide Fuel Cells

Caixia Shi [1,2], Ting Chen [1,*], Dongyang Fang [3] and Shaorong Wang [1,*]

[1] School of Chemistry and Chemical Engineering, China University of Mining and Technology, Xuzhou 221116, China
[2] Xinyi Proton Hydrogen Energy Storage Research Institute, Xuzhou 221400, China
[3] Jiangxi Saici Materials Co., Ltd., Jiujiang 332503, China
* Correspondence: chenting@cumt.edu.cn (T.C.); srwang@cumt.edu.cn (S.W.)

Abstract: In this work, $La_{1-x}Sr_xNi_{0.4}Fe_{0.6}O_{3-\delta}$ ($0 \leq x \leq 0.2$) oxides were synthesized and employed as the identical electrode of direct methane symmetrical solid oxide fuel cell (SSOFC). In addition, the phase structure, redox stability, electrical conductivity, chemical compatibility, and thermal expansion of $La_{1-x}Sr_xNi_{0.4}Fe_{0.6}O_{3-\delta}$ oxides were evaluated. The La_2NiO_4 phase occurs when the amount of doped Sr rises to 0.2. The composition of $La_{0.9}Sr_{0.1}Ni_{0.4}Fe_{0.6}O_{3-\delta}$ (LSNF9146) boasts the highest conductivity of 463 S cm^{-1} with lowest activation energy of 0.066 eV as well as a relatively large thermal expansion coefficient. After treatment in methane for 10 h, the LSNF9146 oxide exhibits 33% lower carbon deposition than the $LaNi_{0.4}Fe_{0.6}O_{3-\delta}$ (LNF46) oxide. Moreover, the impregnated LSNF9146 electrode demonstrates lower polarization resistance in both air and methane atmospheres. SSOFCs with impregnated LSNF9146 and LNF46 identical composite electrodes have the maximum power densities of 233 and 170 mW cm^{-2} at 850 °C in methane, respectively. These results prove that LSNF9146 is a promising symmetrical electrode with high catalytic activity, good redox stability, and coking resistance to direct methane SSOFCs.

Keywords: solid oxide fuel cells; symmetrical electrodes; $La_{1-x}SrxNi_{0.4}Fe_{0.6}O_{3-\delta}$; impregnation; direct methane

Citation: Shi, C.; Chen, T.; Fang, D.; Wang, S. Evaluation of $La_{1-x}Sr_xNi_{0.4}Fe_{0.6}O_{3-\delta}$ as Electrode Materials for Direct Methane Symmetrical Solid Oxide Fuel Cells. *Crystals* **2023**, *13*, 152. https://doi.org/10.3390/cryst13010152

Academic Editors: Fengyu Shen and Yucun Zhou

Received: 22 December 2022
Revised: 12 January 2023
Accepted: 13 January 2023
Published: 15 January 2023

1. Introduction

Fuel cell technology, one of the most promising, environment-friendly, economically expedient and efficient power generation technologies, can meet the ever-increasing requirement for green energy in the 21st century. Solid oxide fuel cells (SOFCs), an electrochemical energy-conversion device, offer tremendous promise for delivering high electrical efficiency and significant environmental benefits in terms of fuel flexibility (hydrocarbons and municipal waste). Moreover, they can generate electricity in a clean and efficient way (>70% with fuel regeneration). Therefore, they have been attracting significant attention in recent years [1,2]. With respect to SOFCs, symmetrical solid oxide fuel cells (SSOFCs), whose anodes and cathodes have the same material, demonstrate great potential for practical application thanks to the simple production procedures, appropriate preparation cost, improved thermomechanical compatibility, and great tolerance to sulfur poisoning and carbon deposition [3,4]. Significant efforts have been devoted to develop symmetrical materials that boast structure stability and desired catalytic activity in both oxidizing and reducing environments, yet it is still challenging to find a suitable electrode which can meet the requirements of anode and cathode in SSOFCs [5,6].

Generally, hydrogen is an ideal fuel which only emits steam. However, hydrogen is expensive since it is produced through water electrolysis, methanol, or methane reforming with further purification. Methane was suggested directly as fuel, which can adjust the reforming process during the electrochemical reaction [7]. However, the deactivation of Ni cermet anode remains the major challenge due to the severe carbon deposition

from methane cracking [8]. Therefore, symmetrical electrode materials with anti-carbon properties are great prospects.

In principle, electrode materials of SSOFCs require a stable lattice structure in both oxidizing and reducing atmospheres. These materials should possess great ionic and electronic conductivity and high electrochemical activity for oxygen-reduction reactions when serving as the cathode; they should be of efficient electrocatalytic activity for methane and hydrogen when acting as the anode. At present, various types (such as ABO_3) of oxides have been applied as the symmetrical electrode in SSOFCs, including $LnCrMO_3$-based (Ln = La, Pr) oxides, $SrFeO_3$-based oxides, $SrTiO_3$-based oxides, and perovskite-type oxides.

Bastidas et al. proposed the concept of SSOFC using $La_{0.75}Sr_{0.25}Cr_{0.5}Mn_{0.5}O_3$ (LSCM) as the electrode material for the first time, and found the maximum power density of 230 mW cm^{-2} at 900 °C in methane fuel with yttria stabilized zirconia (YSZ) electrolyte-supported SOFCs [9]. They concluded that LSCM is a promising alternative material for SSOFCs, displaying a stable phase structure in both oxidizing and reducing atmospheres. Nevertheless, LSCM has low electrical conductivity (1–3 S cm^{-1}) in the temperature range of 750–950 °C, which affects the electrochemical performance of SOFCs [10]. Some Fe or Al-contained (La, Sr) CrO_3 electrodes exhibit better cathodic performance at intermediate temperatures or better hydrocarbon oxidation ability than LSCM oxides [11]. It is generally accepted that B-site cations primarily dictate the catalytic activity of perovskite oxides, but doping in A-site can also affect the catalytic activity indirectly by changing the valence state of B-site. Recently, bismuth-doped LSCM in A-site [12] and titanium-doped LSCM in B-site [13] have demonstrated sound catalytic activity for electrochemical anodic reactions. However, the electrocatalytic activity of methane oxidation of these $LnCrMO_3$-based oxides still requires improvement.

It was verified that $Sr_2Fe_{1.5}Mo_{0.5}O_{6-\delta}$ oxide has remarkable redox stability and good catalytic activity for H_2/CH_4 in SSOFCs [14,15]. Moreover, Xiao et al. explored the possibility of applying $SrFe_{0.75}Mo_{0.25}O_{3-\delta}$ in LSGM-supported SSOFCs [16]. Meanwhile, $SrTiO_3$-based oxides were applied for the high resistance to carbon deposition and sulfur poisoning. Canales-Vázquez et al. reported a symmetrical YSZ-supported single cell with Fe-substituted (La,Sr) TiO_3 ($La_4Sr_8Ti_{12-x}Fe_xO_{38-\delta}$, x = 6.0) electrodes. This single cell shows 100 mW cm^{-2} at 950 °C in H_2 environment [17]. Hanif et al. adopted $La_{0.7}Sr_{0.3}Ti_{0.1}Fe_{0.6}Ni_{0.3}O_{3-\delta}$ as the symmetrical electrode with LSGM electrolyte and obtained 402 mW cm^{-2} at 800 °C [18]. Other Al-doped $SrTiO_3$ [19] and $La_{0.875}Sr_{0.125}Ti_{0.5}Ni_{0.5}O_3$ oxides [20] have also been developed as the symmetrical electrodes of SSOFCs. However, the low electrical conductivity under the reducing atmosphere and insufficient electrocatalytic activity of these $SrTiO_3$-based materials hinder their application in SSOFCs.

Redox reversible oxide, a type of promising electrode, is superior to redox stable materials in preventing large internal strains derived from the different chemical expansion behaviors during redox cycling. It has been widely investigated for the easy precipitation of metal nanoparticles in a reducing atmosphere, thereby enhancing the catalytic activity of anodes. Lanthanum nickelate ($LaNiO_3$) has the advantages of high electrical conductivity, low charge transfer resistance, and good electrocatalytic performance; therefore, it is a promising candidate for SSOFCs [21,22]. Researchers have explored the redox function of iron-doped $LaNiO_3$ ($LaNi_{1-x}Fe_xO_{3-\delta}$) for selective catalytic reduction and hydrogen production in SOFCs [23,24]. $LaNi_{0.6}Fe_{0.4}O_{3-\delta}$ serves as a good cathode material when x = 0.4 in $LaNi_{1-x}Fe_xO_{3-\delta}$. Luo et al. [25] used $LaNi_{0.6}Fe_{0.4}O_{3-\delta}$ as the symmetrical electrode and YSZ as the electrolyte; the single cell they obtained exhibits a maximum power density of 1000 mW cm^{-2} at 800 °C and performs well in both anodic and cathodic atmospheres for SSOFCs. The research of Arandiyan et al. [26] proved the good stability of $LaNi_{1-x}Fe_xO_{3-\delta}$ as an active catalyst for methane CO_2 reforming. Some carbon deposition was found on the waste catalyst. In addition, the catalytic performance of $LaNi_{1-x}Fe_xO_{3-\delta}$ can be easily adjusted by partially substituting La^{3+} cations at the A-site. For example, the doping of Ba^{2+}, Ce^{4+}, or Sr^{2+} can increase the number of ions for achieving high chemical reactivity [27].

Based on the good cathode performance of $LaNi_{0.4}Fe_{0.6}O_{3-\delta}$ (LNF46) and high activity for CO_2 catalytic reforming of CH_4, in this work, doping Sr at the A-site of LNF46 was investigated to grasp chemical reaction activity and anti-carbon deposition behaviors.

In this work, a series of $La_{1-x}Sr_xNi_{0.4}Fe_{0.6}O_{3-\delta}$ ($0 \leq x \leq 0.2$) oxides were synthesized and employed as the identical electrode for direct methane SSOFCs. Furthermore, the properties of phase structure, redox stability, electrical conductivity, chemical compatibility, and thermal expansion of $La_{1-x}Sr_xNi_{0.4}Fe_{0.6}O_{3-\delta}$ oxides were evaluated. In addition, the carbon deposition behaviors of LSNF9146 and LNF46 oxides after reduction in methane atmosphere were analyzed. Both LSNF9146 and LNF46 served as identical electrodes to investigate the electrochemical performance of SSOFCs in methane fuel.

2. Experiments

2.1. Powder Preparation and Characterization

$La_{1-x}Sr_xNi_{0.4}Fe_{0.6}O_{3-\delta}$ (x = 0.00, 0.09, 0.10, 0.15, and 0.20 LSNF) materials were prepared by the citric acid-EDTA sol-gel method [28], the molar ratio of metal ion to citric acid and EDTA being 1:1:1.5. An appropriate amount of $La(NO_3)_3 \cdot 6H_2O$ (AR, aladdin), $Sr(NO_3)_2$ (AR, Tianjin Zhiyuan Chemical Reagent Co., Ltd.), $Ni(NO_3)_2 \cdot 6H_2O$ (AR, aladdin), and $Fe(NO_3)_3 \cdot 9H_2O$ (AR, Sinopharm Group Chemical Reagent Co., Ltd., Shanghai, China) were mixed together in 100 mL of deionized water at stoichiometric proportions. After complete dissolution, the corresponding citric acid and EDTA were added; the final pH of the solution was adjusted to 3~4 by ammonia. Thereafter, the solution was heated and stirred at 80 °C for 30 min for a full mixture and then heated at 120 °C to convert the sol into gel. Subsequently, it was dried at 230 °C for 12 h to obtian the dry precursor, and finally calcined at 1100 °C for 3 h to obtain LSNF composition.

The phase structure of the as-synthesized powders was characterized by the X-ray diffractometer (XRD, D8 ADVANCE from Bruker, Bremen, Germany) with Cu Kα radiation (λ = 1.5408Å). Data were collected in a continuous scan mode in the range of 20–80° with an interval of 0.02°. A representative $La_{0.9}Sr_{0.1}Ni_{0.4}Fe_{0.6}O_{3-\delta}$ (LSNF9146) and LNF46 after heat treatment in CH_4 and oxidization in air were evaluated by means of XRD. For chemical compatibility tests, 10% Sc_2O_3 stabilized ZrO_2 (SSZ, commercial source) and LSNF powder were mixed at a weight ratio of 1:1 and ground uniformly in a mortar; then, they were pressed into tablets. After calcination at 900 and 1100 °C for 10 h respectively, the mixed pellets were subject to XRD analysis.

The electrical conductivity of LSNF was measured by the DC four-probe method with Ag paste electrodes and Ag wires as the current collector in different atmospheres (Air, N_2, and O_2) at 650–850 °C. The samples for thermal expansion coefficient characterization were the same as those for conductivity measurement. The thermal expansion measurement of LSNF was performed with a dilatometer (7MA402, NETZSCH, Selb, Germany) on cuboid specimens in the temperature range of 25–1000 °C in air at a heating rate of 5 K/min. The weight loss behaviors of LSNF9146 and LNF46 after heat treatment at 900 °C in CH_4 atmosphere for 10 h were investigated by thermogravimetry (TG, DSC1 1,100F, Zurich, Switzerland).

2.2. Cell Preparation and Electrochemical Performance Tests

SSOFCs with impregnated LSNF9146 or LNF46 electrode were produced by a two-step procedure (Figure S1). First, the LSNF9146 nitrate solution for impregnation was prepared by dissolving stoichiometric amounts of $La(NO_3)_3 \cdot 6H_2O$, $Sr(NO_3)_2$, $Ni(NO_3)_2 \cdot 6H_2O$, and $Fe(NO_3)_3 \cdot 9H_2O$ with 30% alcohol solution, where citric acid was added at a 1:1 molar ratio to metal ions. Second, the LSNF9146 aqueous solution was infiltrated into porous SSZ backbone (SSZ_{Porous} | SSZ_{Dense} | SSZ_{Porous} symmetrical structure) prepared by tape casting, lamination, hot pressing, and co-sintering. After the drying treatment, heat treatment was conducted in ambient atmosphere at 850 °C for 2 h. The impregnation/heat treatment cycles were repeated to reach the desired amounts of impregnated active material,

57% of the porous SSZ. SSOFCs with LNF46 and LSNF9146 were prepared in accordance with the same procedure.

For electrochemical measurement, silver grids and wires were applied to the $La_{1-x}Sr_xNi_{0.4}Fe_{0.6}$-SSZ electrode surfaces as the current collectors and voltage/current leads. Single cells were sealed to the alumina tubes by silver paste (DAD-87, Shanghai Research Institute of Synthetic Resins, Shanghai, China). The experimental setup of SSOFC can be found in Figure S2. The current-voltage curves and electrochemical impedance spectra (EIS) were obtained at 700–850 °C using a SP-300 Electrochemical Workstation (Bio-Logic, Gottingen, Germany). Ambient air was maintained on the cathodes while 3% H_2O humidified methane was supplied at a flow rate of 30 mL min^{-1} to the anodes. EIS were collected at open circuits over the frequency range of 50–5 MHz with a bias voltage of 10 mV. The EIS of symmetrical cell in air were also studied. Symmetrical anode cell and symmetrical cathode cell shared the same active area of 1.62 cm^2. The morphology and element composition of the LSNF9146 and LNF46 anodes after electrochemical performance were evaluated by scanning electron microscope (SEM, Quanta 250FEI, Hillsboro, OR, USA) with an energy dispersive spectroscopy (EDS) detector.

3. Results and Discussion

3.1. Crystal Structure and Conductivity Properties

Figure 1a shows the XRD spectra of $La_{1-x}Sr_xNi_{0.4}Fe_{0.6}O_{3-\delta}$ (x = 0.00, 0.09, 0.10, 0.15, and 0.20) materials calcined at 1100 °C for 2 h in air atmosphere. When $x \leq 0.15$, notable single perovskite-structure diffraction peaks can be observed yet no impurity peaks appear. When x > 0.15, an extra diffraction peak of $La_2NiO_{4-\delta}$ occurs. The segregation of $La_2NiO_{4-\delta}$ oxide occurs with the increase in the amount of doped Sr^{2+}, indicating that the solubility of Sr reaches the doping limitation [29]. It can be seen from Figure 1b that the diffraction angle of 2θ = 31.5–34° shifts to the right with the rising amount of Sr. When x = 0.1, the shift is the largest; when x = 0.15, the diffraction peak slightly deviates to the direction of the small diffraction angle, indicating an increase in the interplanar spacing. As LSNF (x = 0.00, 0.09, 0.10, and 0.15) are all orthorhombic crystal phases, the unit cell volume under the same crystal phase is proportional to the interplanar spacing. The unit cell volume declines first and then grows with the rise in Sr content when there is no impurity peak. The smallest unit cell volume to LSNF occurs when x = 0.1, consistent with the results in previous studies [30]. This trend is mainly caused by the two charge compensation mechanisms:

$$SrO \xrightarrow{LSNF} Sr'_{La} + Ni, Fe_{Ni,Fe} + O^x_o \quad (1)$$

$$2SrO \xrightarrow{LSNF} 2Sr'_{La} + V\ddot{o} + O_{2(g)} \quad (2)$$

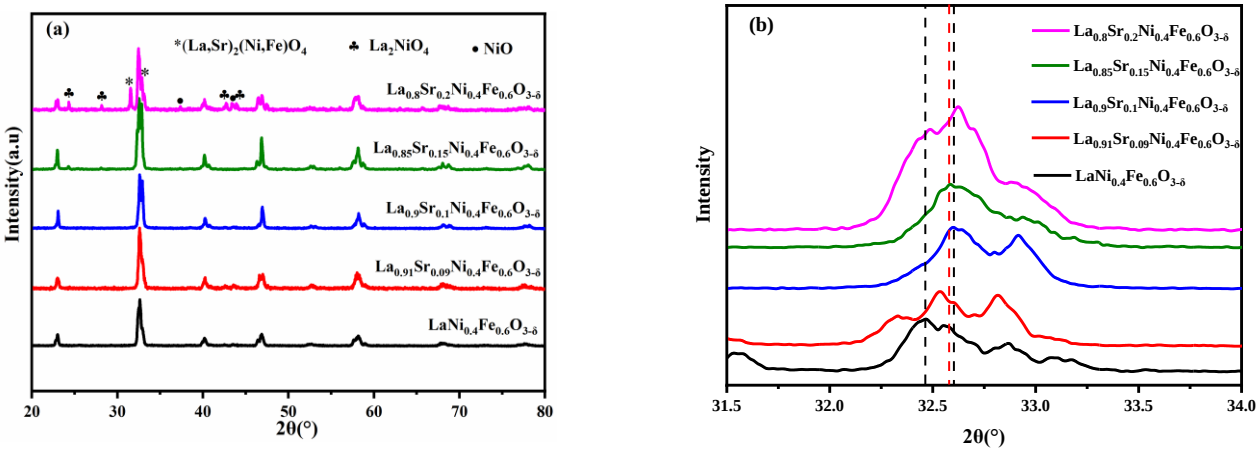

Figure 1. (**a**) XRD spectra and (**b**) partially enlarged XRD peak around 32.5° of $La_{1-x}Sr_xNi_{0.4}Fe_{0.6}O_{3-\delta}$ (x = 0.00, 0.09, 0.1, 0.15, 0.20) materials calcined at 1100 °C for 2 h in air.

Equation (1) is correlated with the charge compensation mechanism. The isomorphic substitution of La^{3+} to Sr^{2+} at the A-site of the perovskite oxidizes cations in the B-site (Ni or Fe) of the structure, thus narrowing the radius of the B cation and contracting cell parameters (these cations in LNF46 without doped Sr are mainly in the +3 valence state) [31,32]. Equation (2) is correlated with the charge compensation mechanism of the introduction of heterovalent bodies. The cation (Sr^{2+} rather than La^{3+}) forms an oxygen vacancy for every two Sr^{2+} ions, and the introduction of Sr^{2+} and the formation of the corresponding oxygen vacancies can be expressed by Equation (2). The cell lattice parameter rises slightly as the ionic radius of Sr^{2+} (0.144 nm) is larger than La^{3+} (0.132 nm). The above mechanisms in the Sr-doped LNF materials can explain the overall characteristics of LSNF materials.

The conductivity and activation energy diagrams of $La_{1-x}Sr_xNi_{0.4}Fe_{0.6}O_{3-\delta}$ (x = 0.00, 0.09, 0.1, 0.15, and 0.20) materials are illustrated in Figure 2. It can be seen from Figure 2a that the conductivity of this material in air does not change significantly as a function over temperature, and the conductivity clearly increases at the beginning and then decreases slightly as the amount of doped Sr exceeds 0.1. The largest conductivity of $La_{1-x}Sr_xNi_{0.4}Fe_{0.6}O_{3-\delta}$ (LSNF9146) is 463 S cm^{-1}, similar to the finding in previous research [30]. When $x \leq 0.1$, it is mainly limited by the oxidation process of B-site cations. As the amount of doped low-valence Sr^{2+} rises (Sr^{2+} to substitute La^{3+}), the oxidation process in B-site cation occurs to maintain electrical neutrality and thereby increase the concentration of small polarons, thus raising electrical conductivity. When $x > 0.1$, it is mainly limited by the formation process of oxygen vacancies. Every two Sr^{2+} ions could form an oxygen vacancy when Sr^{2+} replaces La^{3+}. However, when the oxygen vacancy reaches a certain concentration, the electronic conductivity decreases for lack of bridging between oxygen and cations [30]. Moreover, the activation energies of LSNF verify this trend (Figure 2b). The LSNF9146 oxide shows the lowest E_a of 0.066 eV. Therefore, the composition of LSNF9146 is selected as the electrode material of direct methane fuel SSOFCs in this work according to its relatively high conductivity and low activation energy.

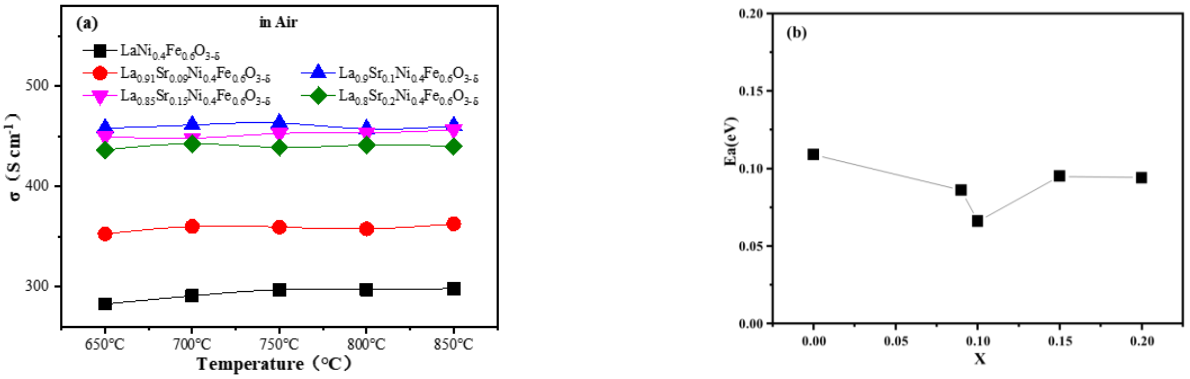

Figure 2. (**a**) Conductivity curves of $La_{1-x}Sr_xNi_{0.4}Fe_{0.6}O_{3-\delta}$ (x = 0.00, 0.09, 0.1, 0.15, and 0.20) oxides at 650–850 °C; (**b**) Relationship between conductivity activation energy (E_a) and the amount of doped Sr.

3.2. Thermal Expansion, Chemical Compatibility, and Carbon Deposition

Figure 3a shows the thermal expansion coefficients of LSNF9146 and SSZ in the temperature range of 25–1000 °C. The thermal expansion coefficient of SSZ is 10.85×10^{-6} K^{-1}, which is close to the previous research (10.0×10^{-6}–10.70×10^{-6} K^{-1}) [33]. The values of LSNF9146 and undoped LNF46 are 15.16×10^{-6} K^{-1} and 12.00×10^{-6} K^{-1} respectively, which is larger than SSZ. Doping Sr in LNF46 can result in a higher thermal expansion coefficient, which is attributed to the transition from orthorhombic phase to rhombohedral phase [28]. The change in thermal expansion coefficient can also reflect the overall bond strength in the perovskite oxide to a certain extent. The change shows that doping Sr weakens the bond strength among ions in the lattice system, which raises the degree of ex-

pansion of the lattice with temperature; namely, it induces an increase in the coefficient. The chemical compatibility between LSNF9146 and SSZ calcined at different temperatures is presented in Figure 3b. The second phase does not occur at 900 °C yet it occurs in $La_2Zr_2O_7$ at 1100 °C. $La_2Zr_2O_7$, an insulating phase, limits the electrical conductivity. Generally, a matched thermal expansion coefficient of cathode material to the typical YSZ or SSZ electrolyte is required to ensure the similar expansion and shrinkage behaviors between the electrolyte and electrodes. In this way, the thermal stress from different layers can be reduced during thermal cycling, thus avoiding delamination or cracks. Considering the mismatched thermal expansion coefficient and reaction at high temperature between SSZ electrolyte and LSNF9146 and LNF46 electrodes, a composite electrode was applied by impregnating LSNF9146 and LNF46 nitrate solution into the porous SSZ backbone and constructing the paths of catalytic process. This method can lower the production temperature and avoid the delamination at the electrode/electrolyte interface induced by the mismatched thermal expansion coefficient, which the traditional screen-printing method fails to solve.

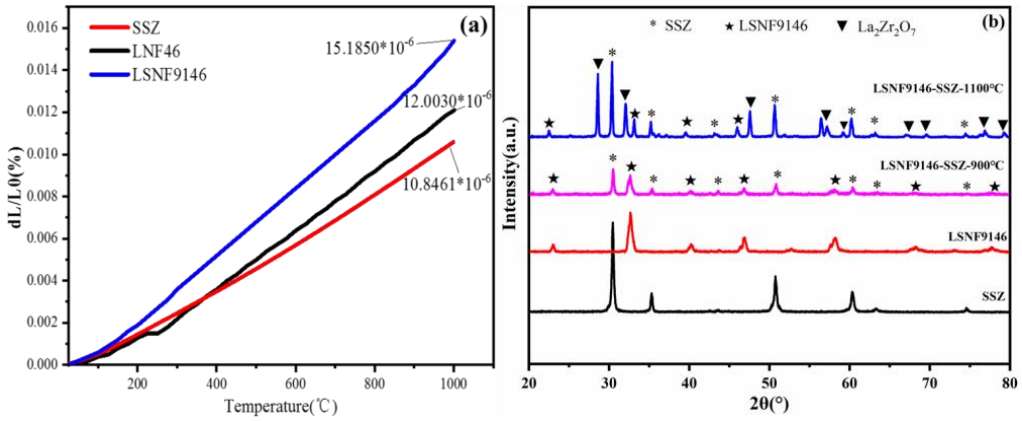

Figure 3. (**a**) Comparison of thermal expansion coefficients of LSNF9146 and SSZ; (**b**) Chemical compatibility between LSNF9146 and SSZ at different sintering temperatures.

Figure 4a summarizes the XRD spectra of LSNF9146 and LNF46 powders thermally treated under different conditions. They are both unstable in CH_4 at a high temperature. After CH_4 treatment at 900 °C for 10 h, La_2O_3, $Sr_2Fe_2O_5$, and $Fe_{0.64}Ni_{0.36}$ are found in both powders, while $La(OH)_3$ only exists in LNF46. These decomposed oxides were then calcined in air for 3 h, respectively; the primitive phase can be recovered. The results demonstrate that LSNF9146 and LNF46 are good redox reversible materials for SSOFC electrodes.

Figure 4b shows the thermogravimetric curves of LSNF9146 and LNF46 powders in air atmosphere after CH_4 treatment at 900 °C for 10 h. The mass change is related to the weight of carbon deposition. The weight losses of LSNF9146 and LNF46 are 35% and 68%, respectively. The results indicate that LSNF9146 performs better for anti-carbon deposition, suggesting that doping Sr in LNF46 contributes to alleviating carbon deposition.

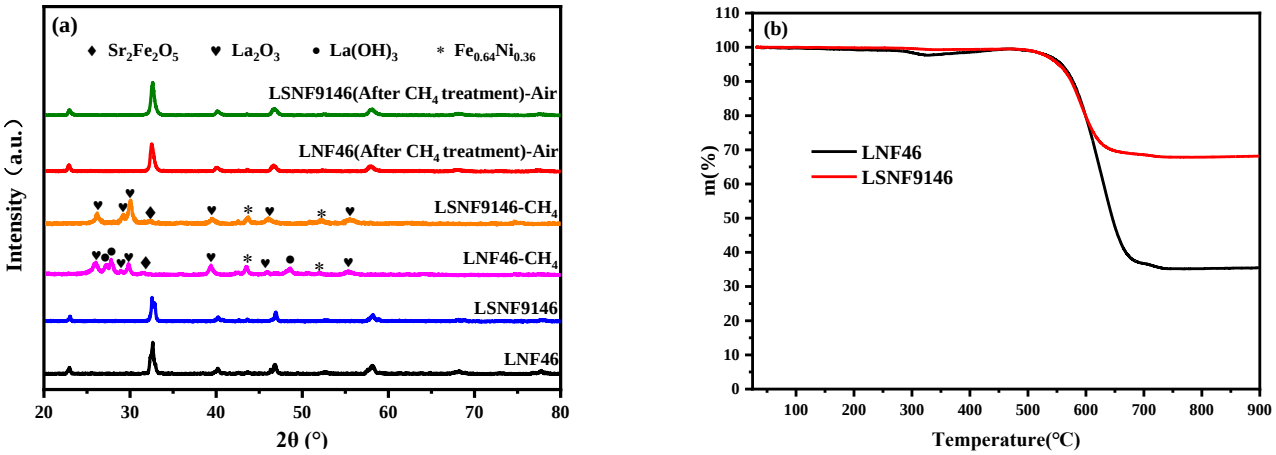

Figure 4. (**a**) XRD spectra of $La_{1-x}Sr_xNi_{0.4}Fe_{0.6}O_{3-\delta}$ (x = 0.00, 0.10) after treatment under different conditions; (**b**) Thermogravimetric analysis on LSNF9146 and LNF46 oxides after CH_4 treatment at 900 °C for 10 h.

3.3. Electrochemical Performance and Microstructure Characterization

To better grasp the performance of electrodes, EIS of symmetrical cells with LSNF9146 and LNF46 electrodes are contrasted (Figure 5). As a cathode material, LSNF9146 electrode has a polarization resistance of 0.06 and 0.10 Ωcm^2 at 850 and 800 °C, respectively (Figure 5a), lower than the LNF46 electrode (0.079 and 0.12 Ωcm^2) (Figure 5b), displaying an excellent catalytic property.

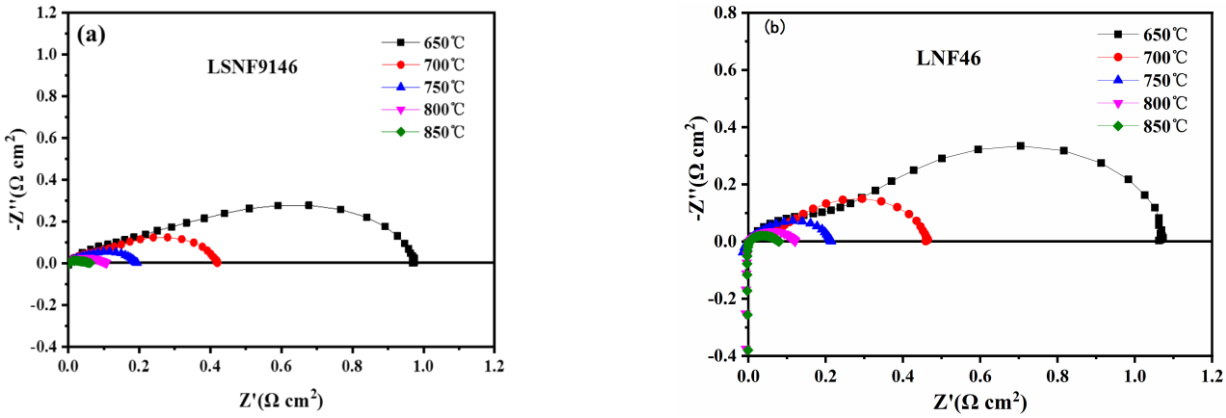

Figure 5. Symmetrical cell performance of (**a**) LSNF9146 and (**b**) LNF46 electrodes in air atmosphere.

During fuel cell measurement, the two impregnated LSNF9146-SSZ and LNF46-SSZ layers were exposed to ambient air oxidants and humidified methane fuels, acting as the cathode and anode, respectively. As illustrated in Figure 6a,c, typical cell voltages and power densities of SSOFCs are a function of current density at 700–850 °C. The maximum power densities of SSOFCs with LSNF9146 are 233, 140, 102, and 66 mW cm^{-2} at 850, 800, 750, and 700 °C, respectively, significantly higher than SSOFCs with LNF46 electrode (170 mW cm^{-2} at 850 °C). The electrolyte-supported SSOFCs with LSNF9146 also perform better than a YSZ-supported symmetrical cell of 78 mW cm^{-2} produced by phase inversion measure in methane fuel [34]. The open-circuit voltage (OCV) of single cells exceeds 1 V and grows as the operating temperature rises due to the increasing entropy for methane oxidation reactions. The OCV of the cell with LSNF9146 is larger than the LNF46 electrode, suggesting a better catalytic activity of LSNF9146 toward methane oxidation. It should be noted that the IVP curves show around 0.6 V at an elevated temperature. It is assumed that the change arises from the impact of concentration polarization and carbon deposition, which shows a similar phenomenon as other SSOFCs measured in direct methane fuel [7,25].

This can be improved by optimizing the microstructure of porous SSZ and the loading amount of catalyst. The corresponding Nyquist plots of impedance data of cells with LSNF9146 and LNF46 electrodes at open circuits are presented in Figure 6b,d, respectively. R_o is ohmic resistance and R_p is polarization resistance of single cells from both anode and cathode. To better present the differences in LSNF9146 and LNF46 electrodes, their power density corresponding to R_o and R_p is summarized in Figure 6e,f. Notable improvement can be observed. The R_p values of SSOFCs with LSNF9146 are 2.65, 1.38, 1, and 0.59 Ω cm^2 at 700, 750, 800, and 850 °C, respectively, significantly lower than the LNF46 electrode. Typically, they share the same R_o, demonstrating the structure stability of SSZ support with electrodes; the slight difference could be attributed to the connecting wires in the testing setup as reported in previous research [35]. To further elaborate on the polarization process of SSOFCs, the EIS curves were analyzed by the distribution of relaxation time (DRT) method. Figure 6g,h shows the DRT results of SSOFCs with LSNF9146 and LNF46 electrodes, respectively. Each deconvolution peak reflects one certain electrochemical process. Generally, it can be expressed that the characteristic frequency of 0.1–10 Hz peak is related to the gas conversion process and the gas diffusion in anode, and the characteristic frequency of 10–100 Hz peak is related to the oxygen surface exchange reaction and gas diffusion within the cathode, while the characteristic frequency of 100–10^4 Hz peak and 10^4–10^5 Hz peak is the charge transfer reaction within the anode and oxygen ionic transport within the cathode, respectively [36]. The area of peaks P2, P3, and P4 in both SSOFCs decreased as the operating temperature increased, indicating the faster oxygen exchange kinetics, charge transfer reaction, and oxygen ionic transport. The P1 of LSNF9146-based SSOFC was shifted to a higher frequency position, but only slightly decreased in the peak area. The P1 and P2 were the main rate-controlling step, which is related to the gas diffusion and gas conversion process in anode and oxygen surface exchange kinetics in cathode when the operating temperature is over 800 °C. In contrast, a peak of P0 was observed in SSOFC with LNF46 electrode when measured at 850 °C, it is suggested that P0 is related to the gas diffusion in anode, which resulted from carbon deposition on the electrode surface that inhibits the diffusion of anode gas. It should be noted that the area of identified P1-P4 in LSNF9146-based SSOFC is significantly lower than the LNF46-based SSOFC, indicating a better anodic and cathodic performance.

With reference to the R_p result of cathode electrode in Figure 5, it can be seen that the anode R_P (derived by subtracting the cathode contributions from the combined interfacial polarization resistances) dominates the main contribution on the total impedance at all temperatures. The anode R_p of the cell of LSNF electrode is about 7 times larger than the cathode, consistent with the finding in other reports [25]. This results from insufficient catalytic oxides after direct methane reactions and limited gas transmission from carbon deposition. The considerable difference in R_p of LSNF9146 and LNF46 electrodes mainly arises from the degree of carbon deposition and active sites after the two electrodes reduce in CH_4 atmosphere. The LNSF9146 anode shows lower carbon deposition, which may be attributed to the formation of active $Fe_{0.64}Ni_{0.36}$ alloy and less active species as well as the presence of $La(OH)_3$.

Figure 7a,b shows the representative SEM images of symmetrical cells without and with impregnated LSNF9146 catalyst, respectively. The thicknesses of porous and dense SSZ layers are about 164 and 28 μm, respectively. Both LSNF9146 and LNF46 anodes exhibit particle agglomeration after the direct-methane test and are tightly coated on the internal surfaces of porous SSZ backbones (Figure 7c,d). The spherical particles of magnified views of LSNF9146 and LNF46 perovskite catalysts are presented in Figure 7e,f, displaying relatively uniform distribution on the electrode surface. The pore size of LSNF9146 is significantly smaller than the LNF46 electrode. It should be noted that the spherical particles might be $Fe_{0.64}Ni_{0.36}$, which corresponds to a longer three-phase interface and more catalytically active sites than the LNF46 electrode. According to Figure S1 (see supplementary materials), LSNF9146 has a good catalytic effect on CH_4 [25], while no spherical particles are observed on the anode surface of LNF9146 electrode. This illustrates

that the Sr-doped LNF electrode material corresponds to a lower particle growth rate than the undoped electrode material. Moreover, it is conducive to the precipitation of nickel-iron alloy which has catalytic activity for CH_4, thereby improving the electrochemical performance of cells under methane fuel.

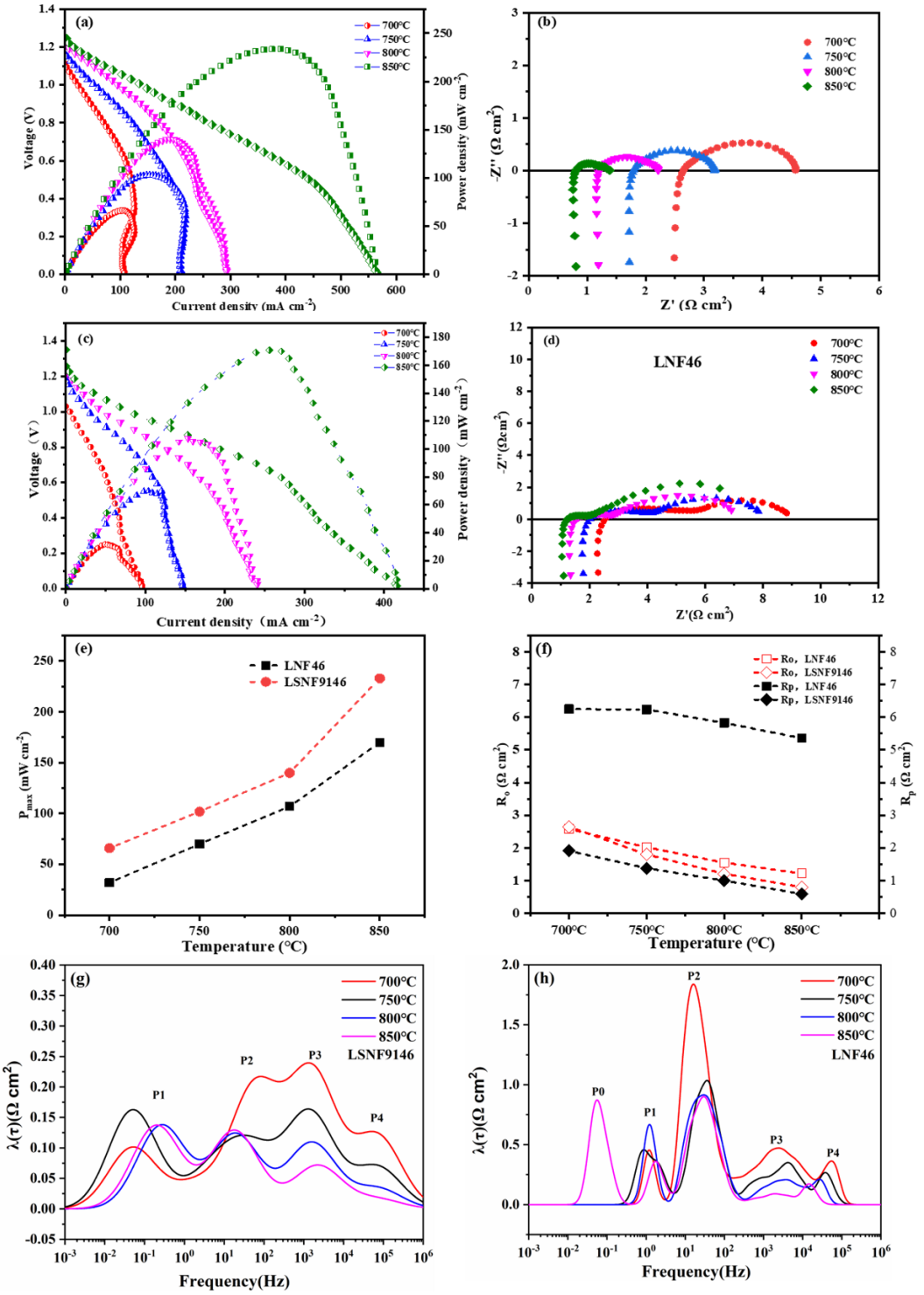

Figure 6. Electrochemical characteristics of symmetrical fuel cells operated in humidified methane fuels at 30 mL min^{-1} and ambient air oxidants over the temperature range of 700–850 °C: (**a**) IVP

curves with LSNF9146 electrode and (**b**) corresponding EIS at open circuits; (**c**) IVP curves with LNF46 electrode and (**d**) corresponding EIS at open circuits; (**e**) Comparison of peak power density (P_{max}) of symmetrical cells with LNF46 and LSNF9146 electrodes at 700–850 °C; (**f**) R_o and R_p of LNF46 and LSNF9146 under the same conditions; (**g**) DRT analysis results of SSOFC with LSNF9146 electrode at elevated temperatures; (**h**) DRT analysis results of SSOFC with LNF46 electrode.

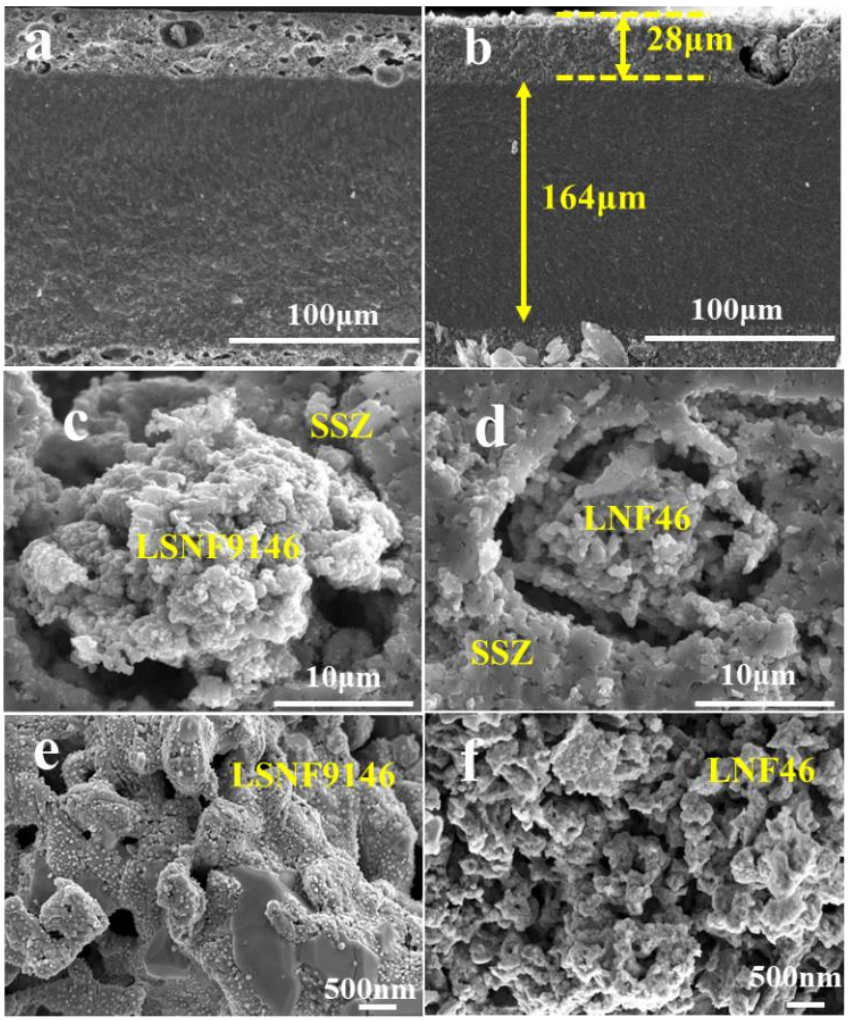

Figure 7. Cross-sectional SEM images of SSZ_{Porous} | SSZ_{Dense} | SSZ_{Porous} structure of (**a**) without impregnation and (**b**) with impregnated LSNF9146; Magnified view of the anodes of (**c**) LSNF9146 and (**d**) LNF46; Magnified view of (**e**) LSNF9146 and (**f**) LNF46 perovskite oxide catalysts after direct methane measurement.

Figure 8 illustrates the cross-sectional views of C distribution in LSNF9146 and LNF46 composite electrodes after electrochemical measurement in methane fuel. C is relatively evenly distributed inside the LSNF9146-infiltrated electrode, while both the inside and surface of LNF46-infiltrated electrode display notable carbon accumulation (Figure 8c,d). Carbon deposition on the anode side can severely deteriorate gas diffusion of cells, thereby increasing the polarization impedance and ultimately suppressing the performance output of cells [37]. The result agrees with the larger polarization impedance of LNF46-infiltrated electrode in Figure 6d. Moreover, the role of C in the LSNF9146 electrode requires further research.

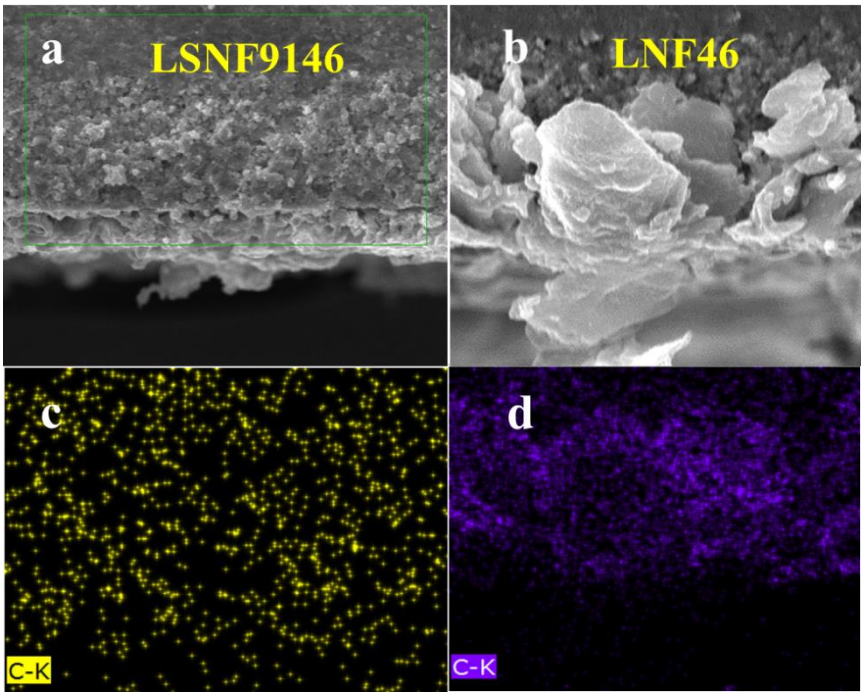

Figure 8. Anode cross-sectional SEM images of (**a**) SSZ-infiltrated LSNF9146 composite electrode and (**b**) SSZ-infiltrated LNF46 composite electrode after tests; Corresponding EDS elemental distribution of C (**c**) in LSNF9146 electrode and (**d**) in LNF46 composite electrode.

4. Conclusions

In this study, a series of $La_{1-x}Sr_xNi_{0.4}Fe_{0.6}O_{3-\delta}$ (x = 0.00, 0.09, 0.10, 0.15, and 0.20) materials were synthesized. The phase structures of LSNF9146 and LNF46 can be recovered after treatment in CH_4 for 10 h and then in air for 3 h at 900 °C, which presents remarkable redox stability. LSNF9146 demonstrates a higher electrical conductivity and a larger thermal expansion coefficient than other compositions. Additionally, the symmetrical single cells with structures of LSNF9146-SSZ | SSZ | LSNF9146-SSZ and LNF46-SSZ | SSZ | LNF46-SSZ were successfully prepared. SSOFCs with LSNF9146 electrode using humidified CH_4 as fuel and ambient air exhibit a significantly improved maximum power density compared with the LNF46 electrode: 233, 144, and 102 mW cm^{-2} at 850, 800, and 750 °C, respectively. LSNF9146 demonstrates 33% alleviation of carbon deposition compared with LNF46, and the EDS analysis on LSNF9146 confirms the lower carbon deposition in LSNF9146 electrode after measurement in CH_4, which may result from the different numbers of active species of $Fe_{0.64}Ni_{0.36}$ alloy and less active species of $La(OH)_3$ in LSNF9146 and LNF46. The results can offer a promising redox reversible electrode material for direct methane SSOFC with low carbon deposition. Moreover, its stability shall be investigated in future work.

Supplementary Materials: The following supporting information can be downloaded at: https://www.mdpi.com/article/10.3390/cryst13010152/s1. Figure S1: The skeleton of the symmetrical porous SSZ/ dense SSZ/ porous SSZ with LSNF9146 or LNF46 nanoparticle; Figure S2: The experimental setup of SSOFC.

Author Contributions: Conceptualization, S.W.; methodology, C.S.; validation, D.F., T.C. and S.W.; formal analysis, C.S.; investigation, C.S. and T.C.; data curation, C.S. and D.F.; writing—original draft preparation, C.S.; writing—review and editing, T.C. and S.W.; supervision, S.W.; project administration, S.W.; funding acquisition, T.C. and S.W. All authors have read and agreed to the published version of the manuscript.

Funding: This research was funded by the National Natural Science Foundation of China (52202334) and (51836004), and the Science and Technology Innovation Foundation of Jiangsu Province for Carbon Neutrality (No. BK20220011).

Data Availability Statement: No applicable.

Acknowledgments: We gratefully acknowledge the financial support from the National Natural Science Foundation of China (52202334) and (51836004) and Science and Technology Innovation Foundation of Jiangsu Province for Carbon Neutrality (No. BK20220011).

Conflicts of Interest: The authors declare no conflict of interest.

References

1. Mahmud, L.S.; Muchtar, A.; Somalu, M.R. Challenges in fabricating planar solid oxide fuel cells: A review. *Renew. Sustain. Energy Rev.* **2017**, *72*, 105–116. [CrossRef]
2. Chau, K.; Djire, A.; Khan, F. Review and analysis of the hydrogen production technologies from a safety perspective. *Int. J. Hydrog. Energy* **2022**, *47*, 13990–14007. [CrossRef]
3. Zhang, M.; Du, Z.; Zhang, Y.; Zhao, H. Progress of Perovskites as Electrodes for Symmetrical Solid Oxide Fuel Cells. *ACS Appl. Energy Mater.* **2022**, *11*, 13081–13095. [CrossRef]
4. Ruiz-Morales, J.C.; Marrero-López, D.; Canales-Vázquez, J.; Irvine, J.T.S. Symmetric and reversible solid oxide fuel cells. *RSC Adv.* **2011**, *1*, 1403–1414. [CrossRef]
5. Su, C.; Wang, W.; Liu, M.; Tadé, M.O.; Shao, Z. Progress and Prospects in Symmetrical Solid Oxide Fuel Cells with Two Identical Electrodes. *Adv. Energy Mater.* **2015**, *5*, 1500188. [CrossRef]
6. Yu, J.; Luo, L.; Cheng, L.; Wang, L.; Xia, C.; Xu, X.; Yu, Y. Progress in the Development of Materials of Solid Oxide Fuel Cells. *J. Ceram.* **2020**, *41*, 613–626. [CrossRef]
7. Bian, L.; Duan, C.; Wang, L.; O'Hayre, R.; Cheng, J.; Chou, K.-C. Ce-doped $La_{0.7}Sr_{0.3}Fe_{0.9}Ni_{0.1}O_{3-\delta}$ as symmetrical electrodes for high performance direct hydrocarbon solid oxide fuel cells. *J. Mater. Chem. A* **2017**, *5*, 15253–15259. [CrossRef]
8. Park, S.; Vohs, J.M.; Gorte, R.J. Direct oxidation of hydrocarbons in a solid-oxide fuel cell. *Nature* **2000**, *404*, 265–267. [CrossRef] [PubMed]
9. Bastidas, D.M.; Tao, S.; Irvine, J.T.S. A symmetrical solid oxide fuel cell demonstrating redox stable perovskite electrodes. *J. Mater. Chem.* **2006**, *16*, 1603–1605. [CrossRef]
10. Kharton, V.; Tsipis, E.; Marozau, I.; Viskup, A.; Frade, J.; Irvine, J. Mixed conductivity and electrochemical behavior of $(La_{0.75}Sr_{0.25})_{0.95}Cr_{0.5}Mn_{0.5}O_{3-\delta}$. *Solid State Ion.* **2007**, *178*, 101–113. [CrossRef]
11. Chen, M.; Paulson, S.; Thangadurai, V.; Birss, V. Sr-rich chromium ferrites as symmetrical solid oxide fuel cell electrodes. *J. Power Sources* **2013**, *236*, 68–79. [CrossRef]
12. Zhang, S.; Wan, Y.; Xu, Z.; Xue, S.; Zhang, L.; Zhang, B.; Xia, C. Bismuth doped $La_{0.75}Sr_{0.25}Cr_{0.5}Mn_{0.5}O_{3-\delta}$ perovskite as a novel redox-stable efficient anode for solid oxide fuel cells. *J. Mater. Chem. A* **2020**, *8*, 11553–11563. [CrossRef]
13. Karim, A.; Abdalla, A.; Park, J.-Y.; Petra, P.; Azad, A. Effects of Ti doping on the electrochemical performance of $(La_{0.75}Sr_{0.25})(Mn_{0.5}Cr_{0.5})O_{3-\delta}$ anode for solid oxide fuel cells. *Process. Appl. Ceram.* **2019**, *13*, 342–348. [CrossRef]
14. Liu, Q.; Dong, X.; Xiao, G.; Zhao, F.; Chen, F. A novel electrode material for symmetrical SOFCs. *Adv. Mater.* **2010**, *22*, 5478–5482. [CrossRef] [PubMed]
15. Liu, Q.; Xiao, G.; Howell, T.; Reitz, T.L.; Chen, F. A Novel Redox Stable Catalytically Active Electrode for Solid Oxide Fuel Cells. *ECS Trans.* **2011**, *35*, 1357–1366. [CrossRef]
16. Xiao, J.; Han, D.; Yu, F.; Zhang, L.; Liu, J.; Zhan, Z.; Zhang, Y.; Dong, P. Characterization of symmetrical $SrFe_{0.75}Mo_{0.25}O_{3-\delta}$ electrodes in direct carbon solid oxide fuel cells. *J. Alloys Compd.* **2016**, *688*, 939–945. [CrossRef]
17. Canales-Vázquez, J.; Ruiz-Morales, J.C.; Marrero-López, D.; Peña-Martínez, J.; Núñez, P.; Gómez-Romero, P. Fe-substituted $(La,Sr)TiO_3$ as potential electrodes for symmetrical fuel cells (SFCs). *J. Power Sources* **2007**, *171*, 552–557. [CrossRef]
18. Hanif, M.B.; Gao, J.-T.; Shaheen, K.; Wang, Y.-P.; Yasir, M.; Zhang, S.-L.; Li, C.-J.; Li, C.-X. Performance evaluation of highly active and novel $La_{0.7}Sr_{0.3}Ti_{0.1}Fe_{0.6}Ni_{0.3}O_{3-\delta}$ material both as cathode and anode for intermediate-temperature symmetrical solid oxide fuel cell. *J. Power Sources* **2020**, *472*, 228498. [CrossRef]
19. Shah, M.A.K.Y.; Lu, Y.; Mushtaq, N.; Yousaf, M.; Rauf, S.; Asghar, M.I.; Lund, P.D.; Zhu, B. Perovskite Al-SrTiO3 semiconductor electrolyte with superionic conduction in ceramic fuel cells. *Sustain. Energy Fuels* **2022**, *6*, 3794–3805. [CrossRef]
20. Arrivé, C.; Delahaye, T.; Joubert, O.; Gauthier, G.H. Study of $(La,Sr)(Ti,Ni)O_{3-\delta}$ materials for symmetrical Solid Oxide Cell electrode—Part C: Electrical and electrochemical behavior. *Ceram. Int.* **2020**, *46*, 23442–23456. [CrossRef]
21. Nam-In, K.; Jin, S.Y.; Sup, Y.T.; Ryul, C.S.; Arslan, A.R.; Taekjib, C.; Young-Soo, S.; Kug-Seung, L.; Yeon, H.J.; Seok, C.W.J.S.A. Oxygen-deficient triple perovskites as highly active and durable bifunctional electrocatalysts for oxygen electrode reactions. *Sci. Adv.* **2018**, *4*, eaap9360.
22. Gozzo, C.B.; Soares, M.; Sczancoski, J.C.; Nogueira, I.C.; Leite, E.R. Investigation of the electrocatalytic performance for oxygen evolution reaction of Fe-doped lanthanum nickelate deposited on pyrolytic graphite sheets. *Int. J. Hydrog. Energy* **2019**, *44*, 21659–21672. [CrossRef]
23. Niwa, E.; Uematsu, C.; Hashimoto, T. Sintering temperature dependence of conductivity, porosity and specific surface area of $LaNi_{0.6}Fe_{0.4}O_3$ ceramics as cathode material for solid oxide fuel cells—Superiority of Pechini method among various solution mixing processes. *Mater. Res. Bull.* **2013**, *48*, 1–6. [CrossRef]

24. Luo, Y.; Wang, X.; Qian, Q.; Chen, Q.J. Studies on B sites in Fe-doped $LaNiO_3$ perovskite for SCR of NOx with H_2. *Int. J. Hydrog. Energy* **2014**, *39*, 15836–15843. [CrossRef]
25. Luo, T.; Liu, X.; Meng, X.; Wu, H.; Wang, S.; Zhan, Z.J.J.o.P.S. In situ formation of $LaNi_{0.6}Fe_{0.4}O_{3-\delta}$–carbon nanotube hybrids as anodes for direct-methane solid oxide fuel cells. *J. Power Sources* **2015**, *299*, 472–479. [CrossRef]
26. Arandiyan, H.; Li, J.; Ma, L.; Hashemnejad, S.M.; Mirzaei, M.Z.; Chen, J.; Chang, H.; Liu, C.; Wang, C.; Chen, L. Methane reforming to syngas over $LaNi_xFe_{1-x}O_3$ ($0 \leq x \leq 1$) mixed-oxide perovskites in the presence of CO2 and O2. *J. Ind. Eng. Chem.* **2012**, *18*, 2103–2114. [CrossRef]
27. Lee, Y.; Suntivich, J.; May, K.J.; Perry, E.E.; Shao-Horn, Y.J. Synthesis and Activities of Rutile IrO_2 and RuO_2 Nanoparticles for Oxygen Evolution in Acid and Alkaline Solutions. *J. Phys. Chem. Lett.* **2015**, 399–404. [CrossRef]
28. Samat, A.A.; Jais, A.A.; Somalu, M.R.; Osman, N.; Muchtar, A.; Lim, K.L. Technology. Electrical and electrochemical characteristics of $La_{0.6}Sr_{0.4}CoO_{3-\delta}$ cathode materials synthesized by a modified citrate-EDTA sol-gel method assisted with activated carbon for proton-conducting solid oxide fuel cell application. *J. Sol-Gel Sci. Technol.* **2018**, *86*, 617–630. [CrossRef]
29. Zhan, G.; Mao, Z.; Cheng, W.; Liu, Z. Preparation and characterization of $La_xSr_xNi_yFe_yO_\delta$ cathodes for low-temperature solid oxide fuel cells. *Int. J. Hydrog. Energy* **2010**, *35*, 12905–12910.
30. Montini, T.; Bevilacqua, M.; Fonda, E.; Casula, M.F.; Fornasiero, P. Relationship between electrical behavior and structural characteristics in Sr-doped $LaNi_{0.6}Fe_{0.4}O_{3-\delta}$ mixed oxides. *Chem. Mater.* **2009**, *21*, 1768–1774. [CrossRef]
31. Bevilacqua, M.; Montini, T.; Tavagnacco, C.; Fonda, E.; Fornasiero, P.; Graziani, M. Preparation, Characterization, and Electrochemical Properties of Pure and Composite $LaNi_{0.6}Fe_{0.4}O_{3-\delta}$Based Cathodes for IT-SOFC. *Chem. Mater.* **2007**, *19*, 5926–5936. [CrossRef]
32. Falcón, H.; Goeta, A.E.; Punte, G.; Carbonio, R.E. Crystal Structure Refinement and Stability of $LaFe_xNi_{1-x}O_3$Solid Solutions. *J. Solid State Chem.* **1997**, *133*, 379–385. [CrossRef]
33. Mizutani, Y.; Tamura, M.; Kawai, M.; Yamamoto, O. Development of high-performance electrolyte in SOFC. *Solid State Ion.* **1994**, *72*, 271–275. [CrossRef]
34. Gu, Y.; Zhang, Y.; Ge, L.; Zheng, Y.; Chen, H.; Guo, L. YSZ electrolyte support with novel symmetric structure by phase inversion process for solid oxide fuel cells. *Energy Convers. Manag.* **2018**, *177*, 11–18. [CrossRef]
35. Han, D.; Liu, X.; Zeng, F.; Qian, J.; Wu, T.; Zhan, Z. A micro-nano porous oxide hybrid for efficient oxygen reduction in reduced-temperature solid oxide fuel cells. *Sci. Rep.* **2012**, *2*, 1–5. [CrossRef]
36. Cui, T.; Li, H.; Lyu, Z.; Wang, Y.; Han, M.; Sun, Z.; Sun, K. Identification of Electrode Process in Large-size Solid Oxide Fuel Cell. *Acta Phys. Chim. Sin.* **2020**, *38*, 2011009. [CrossRef]
37. Wang, D.; Wong, S.I.; Sunarso, J.; Xu, M.; Wang, W.; Ran, R.; Zhou, W.; Shao, Z. A Direct n-Butane Solid Oxide Fuel Cell Using $Ba(Zr_{0.1}Ce_{0.7}Y_{0.1}Yb_{0.1})_{0.9}Ni_{0.05}Ru_{0.05}O_{3\text{-delta}}$ Perovskite as the Reforming Layer. *ACS Appl. Mater. Interfaces* **2021**, *13*, 20105–20113. [CrossRef]